ELSEVIER

Journal of Fluids and Structures 20 (2005) 331–344

JOURNAL OF FLUIDS AND STRUCTURES

www.elsevier.com/locate/jfs

Dynamics of the helical flow between rotating conical cylinders

M.N. Noui-Mehidi[a,*], N. Ohmura[b], K. Kataoka[b]

[a]*Energy and Thermofluids Engineering, CSIRO Manufacturing and Infrastructure Technology, P.O. Box 56, Highett, Vict. 3190, Australia*

[b]*Department of Chemical Science and Engineering, Kobe University, Rokkodai, Nada Kobe 657-8501, Japan*

Received 9 August 2004; accepted 23 December 2004

Abstract

The stability of the helical flow in a system of coaxial rotating conical cylinders, the inner one rotating and the outer one stationary was experimentally investigated. The helical flow resulted from a Hopf bifurcation, which occurred only when the acceleration of the inner conical cylinder was smaller than 0.06 rad/s^2. When the rotational speed of the inner conical cylinder was increased, the transition to turbulence occurred following a succession of flow states: (i) three-dimensional laminar flow (TDLF), (ii) laminar periodic helical flow (LPHF), (iii) doubly periodic wavy helical flow (DWHF), (iv) weakly turbulent helical flow (WTHF) and (v) fully turbulent helical flow (FTHF). Time series obtained by an electrochemical method permitted the identification and analysis of the fundamental frequencies and their evolutions associated with each time-dependent flow state, using Fourier and wavelet transforms. Phase space analysis revealed the associated attractors constructed from the embedded time series. In the FTHF flow state, the fundamental frequency of the helical flow was observed to have a ratio to the rotational frequency of almost twice that of the one measured in the LPHF regime.

© 2005 Elsevier Ltd. All rights reserved.

1. Introduction

In the last decade, Taylor vortices in the flow between two coaxial rotating conical cylinders have been studied both experimentally and numerically by several authors. Wimmer (1995) investigated the occurrence of Taylor vortices in different gap configurations between conical cylinders. He also observed unsteady flow modes, depending on the flow history, which led to helical flows propagating from the largest radius to the smallest when the inner conical cylinder was rotated and the outer one was fixed. Noui-Mehidi and Wimmer (1999) studied the flow states occurring in the presence of a free surface in the same flow system. They obtained a combination of unsteady flow modes, which were only observed in the Taylor–Couette system when both cylinders were rotating in opposite directions. In a numerical analysis, Hoffmann and Busse (1999) showed that a transition from Taylor vortex instabilities to Ekman-type instability occurred at a cone angle of 45°. Wimmer (2000) confirmed this result by a series of experiments using different conical systems. Noui-Mehidi et al. (2001) analyzed the effect of the acceleration rate β of the inner conical cylinder on the different flow modes observed when the Reynolds number, Re, was increased. A flow map plotted in the (Re, β) plane clearly showed the existence of a bifurcation branching occurring after the first Taylor vortices were

*Corresponding author. Tel.: +61 3 9252 6075; fax: +61 3 9252 6252.
E-mail address: Nabil.Noui-Mehidi@csiro.au (M.N. Noui-Mehidi).

0889-9746/$ - see front matter © 2005 Elsevier Ltd. All rights reserved.
doi:10.1016/j.jfluidstructs.2004.12.001

Nomenclature

a	wavelet transform dilatation parameter
C	wavelet transform ($= -(1/\sqrt{a})\int_{-\infty}^{+\infty} \psi((t-\tau)/a)s(t)\,\mathrm{d}t$)
d	gap width
DWHF	doubly periodic wavy helical flow
f_1	helical motion fundamental frequency
f_2	wavy motion fundamental frequency
f_r	inner conical cylinder rotation frequency
FTHF	Fully turbulent helical flow
FTV	first observed vortices
L	fluid column height
LPHF	Laminar periodic helical flow
Re	Reynolds number ($= R_{ih}\Omega d/\nu$)
R_{ih}	inner conical cylinder upper radius
R_{oh}	outer conical cylinder upper radius
$s(t)$	normalized fluctuation component of the signal ($= (S(t) - S_{\mathrm{mean}})/\mathrm{SD}$)
$S(t)$	total recorded signal
S_{mean}	mean component of the signal
SD	standard deviation of the signal
t	time
Δt	sampling time
T	embedding time delay
TDLF	basic three-dimensional laminar flow
UTV	upward traveling motion
WTHF	weakly turbulent helical flow

Greek letters

β	acceleration rate
Γ	aspect ratio ($= L/d$)
η	radius ratio ($= R_{ih}/R_{oh}$)
ν	dynamic viscosity
τ	wavelet transform time shift
ϕ	conical apex angle
ψ	mother "Mexican hat" wavelet($= (1-t^2)\exp(-t^2/2)$)
Ω	inner conical cylinder angular rotational speed ($= \beta t$)

observed, depending on the values of β and Re. On the first branch, a helical flow was observed for acceleration rates $\beta < 0.06\,\mathrm{rad/s^2}$, and it initiated always at the largest radius. On the second branch, for $\beta > 0.06\,\mathrm{rad/s^2}$, a succession of other flow modes was observed. Noui-Mehidi et al. (2002) studied the flow mode selection following the second bifurcation branch, which resulted in an upward travelling flow, followed by steady Taylor vortices and wavy Taylor vortices when Re was increased.

Helical and spiral structures have been observed in a Taylor–Couette system when both cylinders were counter-rotating. Andereck et al. (1986) identified a succession of different flow states during the transition to turbulence. They classified the flow states resulting from spiral-type instability as interpenetrating laminar spirals, wavy interpenetrating spirals, an intermittency region, a transition region and, finally spiral turbulence. Nonlinear spirals have been numerically studied in a Taylor–Couette system by several authors (Antonijoan et al., 1998; Hoffmann and Lücke, 2000; Meseguer and Marquès, 2000). These studies pointed out the complexity of this flow state in circular cylinder systems and its dependency on different dynamical and geometrical parameters.

The present work is concerned with an experimental investigation of the transition to turbulence of the helical flow observed between conical cylinders following the first bifurcation branch, as described above (for $\beta < 0.06\,\mathrm{rad/s^2}$). The flow properties were investigated by Fourier and wavelet analysis of time series recorded for the different observed flows. Dynamical analysis of the time series permitted the identification of the type of bifurcations leading to turbulence.

2. Experimental procedures

2.1. Experimental set-up

The experimental apparatus consisted of two concentric conical cylinders, the inner one was set in rotating motion, while the outer one was at rest. The outer conical cylinder was made of transparent acrylic plastic and the inner conical cylinder of stainless steel (Fig. 1). The upper radii of the inner and outer bodies were equal to $R_{ih} = 42\,\mathrm{mm}$ and $R_{oh} = 50\,\mathrm{mm}$, respectively. Both conical cylinders had the same apex angle of $\phi = 16^\circ$, with the resulting constant gap width $d = 8\,\mathrm{mm}$. At the top of the flow system, the radius ratio was $\eta = R_{ih}/R_{oh} = 0.84$, and the system aspect ratio was $\Gamma = L/d = 15.62$, where L is the fluid column vertical length. The top end-plate was attached to the apparatus lid and the bottom end-plate was fixed to the outer conical cylinder. The basic working fluid was an aqueous solution, as will be discussed in the following section. For the purpose of flow visualization, 2% of Kalliroscope AQ 1000 was added to the

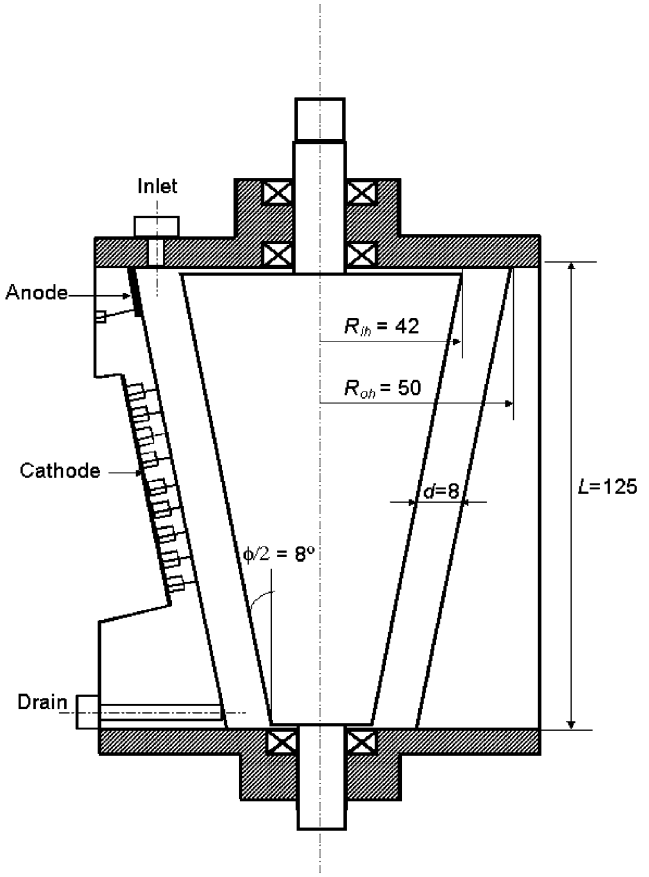

Fig. 1. Experimental apparatus and notations (dimensions in mm).

working fluid. The flow could be observed by both Argon laser cross-section illumination and direct reflected white light.

The inner conical cylinder was able to reach very high rotational speeds by means of a computer-controlled DC motor. The rotational speed was increased linearly following $\Omega(t) = \beta t$, where Ω is the angular velocity, t is time and β the acceleration rate. The Reynolds number, estimated with an accuracy better than 2.5%, has been defined at the upper base for the largest radius as

$$\mathrm{Re} = \frac{R_{ih}\Omega d}{v}, \tag{1}$$

where v is the fluid kinematic viscosity and Ω is the rotational speed of the inner conical cylinder.

2.2. Measuring method

Polarography was used to study the local flow properties in the present investigation. This electrochemical method has been adapted to the study of Taylor–Couette flow systems since the early 1970s by Cognet (1971). The method is based on a simple model of mass transfer. By imposing a potential to the measuring electrode probe that is different from the one of the electrolyte oxydo-reduction equilibrium, the probe active surface in contact with the solution becomes the site of ion exchange. The motion of the ions is the result of the migration motion due to the electrical field, the convection of the flow circulation and the molecular diffusion due to the difference of concentrations between the solution and the electrode. The local current collected at the electrode is proportional to the gradient of the velocity field at the electrode.

The electrolyte used in the present investigation was an aqueous solution of ferri-potassium cyanide at a concentration of 10^{-2} mol/L and ferro-potassium cyanide at an equal concentration of 10^{-2} mol/L. The addition of an excess of an inactive electrolyte, namely potassium nitrate, at a concentration of 1 mol/L permitted the elimination of ion migration in the solution. The motion of ions was then due only to flow convection. The addition of the Kalliroscope AQ 1000 for flow observation increased the fluid kinematic viscosity by only 2%. On the other hand, the Kalliroscope was neutral to the electrochemical solution, thus both flow visualization and signal analysis could be conducted simultaneously. The experimental room was air-conditioned to keep the temperature constant at 25 °C. The controlled long-term room temperature variations were lower than 0.5 °C for all measurement sequences. In order to ensure the accuracy of the working fluid temperature, a thermocouple of copper-constantan, which had an accuracy of better than 0.1 °C, was used. The fluid temperature was measured before and after each experiment and was found to vary by no more than 1 °C. The fluid kinematic viscosity v was found to be 0.97 cS at 25 °C.

A total of nine platinum micro-electrodes of 0.5 mm diameter each were used in the present investigation. The electrodes were set along a vertical line on the inner side of the outer conical cylinder wall. The first top electrode was located 20 mm lower than the top end-plate and the last electrode was located 26 mm above the bottom end-plate to avoid end-plate effects. All electrodes were separated from each other, two by two, by an equal interval of 10 mm. The anode was a square platinum plaque of 15×15 mm fixed to the inner side of the outer conical cylinder near the apparatus lid. The difference of potential was imposed by the use of a DC battery between the anode and the cathode subject to measurement. The potential drop at the ends of a resistance connected to the cathode was amplified with a YOKOGAWA 3133 DC amplifier and then recorded via a TEAC DR-F3 digital recorder where the signal could be visualized on screen. The sampling frequency and the number of recorded samples were set on the digital recorder unit. A total of 4096 readings were recorded for each time-series sample with different sampling frequencies, depending on the nature of the signal related to the observed flow state. When the desired Reynolds number was reached, signal measurements were done after a time equivalent to 100 times the acceleration duration. The steady state could be assessed when the same statistically mean current and the same spectral properties were obtained for each of the sampled time series collected at the same flow regime.

2.3. Signal analysis

Time series collected at the electrode were analyzed by Fourier transform, wavelet transform and reconstruction of attractors in phase space. The signal analysis was performed on the normalized fluctuating component of each recorded time series following the equation:

$$s(t) = \frac{S(t) - S_{\text{mean}}}{\text{SD}}, \tag{2}$$

where $S(t)$ is the total signal recorded, S_{mean} is the mean component of the signal, and SD is the conventional standard deviation.

The power spectra obtained by an FFT algorithm permitted the determination of the characteristic frequencies related to each of the flow states observed.

Wavelet analysis has been recently introduced as an alternative to Fourier transform. While Fourier analysis yields the energy density in individual frequency ranges without estimation with time, wavelet analysis permits the tracking of the spatio-temporal evolution of the signal in various time scales. The wavelet transform of continuous signal $s(t)$ is given by

$$C(\tau, a) = -\frac{1}{\sqrt{a}} \int_{-\infty}^{+\infty} \psi\left(\frac{t-\tau}{a}\right) s(t)\, \mathrm{d}t, \tag{3}$$

where ψ is the mother wavelet, which is an absolutely integrable function. Wavelet analysis is performed by the dilatation and translation of the mother wavelet. The parameter a is related to the dilatation and τ is the time-shift parameter. In the present study the 'Mexican hat function' given by

$$\psi(t) = \left(1 - t^2\right) \exp\left(-\frac{t^2}{2}\right) \tag{4}$$

was chosen as the mother wavelet. Zheng et al. (2001) showed that this mother wavelet was suitable for detecting unsteady local fluctuations. Park et al. (2001) noted that the scaling in the wavelet analysis represents performing stretching and compressing operations on the mother wavelet to detect the frequency information contained in the signal. The compression operation permits the analysis of high-frequency components, while stretching is related to low-frequency components. In the present study, the wavelet transforms are plotted in time-scale graphs where the

wavelet coefficients are normalized by dividing them by the maximal wavelet coefficient value. The iso-correlations are plotted in contour lines representing contour levels from 0 to 1 with an increment step of 0.1.

Embedding time series of the normalized fluctuation $s(t)$ corresponding to a certain flow regime allowed the identification of the associated attractor in the space phase. The process of embedding a signal $s(t)$ corresponds to the construction of a set of signals $s(t+T)$, $s(t+2T)$, $s(t+2T),\ldots,s(t+(n-1)T)$ shifted from the original signal $s(t)$. Although the definition of the time delay T is arbitrary, some methods have been proposed for the evaluation of T. The method of mutual information proposed by Fraser and Swinney (1986) has been used in the present work to estimate the time delay of each time series recorded to construct the associated attractor. In this method the appropriate time delay is the one which corresponds to the first minimum value of the mutual information function $I(t)$ defined by Fraser and Swinney (1986). A Fortran algorithm based on the proposed method permitted the calculation of the time delays for each measured time series. Poincaré sections were taken at the intersection of a specific plane and the constructed attractor in the 3-D phase space defined by $s(t)$, $s(t+T)$ and $s(t+2T)$.

3. Transition sequence

3.1. Basic flow and first instability

The variation of the centrifugal forces due to the axial change of the conical radii yields a nonuniform dynamical field along the fluid column, even when the gap width is axially constant when both conical cylinders have the same apex angle. This property has a major effect on the transition from the laminar state to turbulence since the basic laminar flow (abbreviated as TDLF) is three dimensional.

Fig. 2 presents a diagram summarizing the different flow states obtained when the acceleration rate changes at the first flow bifurcations. The first critical Reynolds number $\mathrm{Re}_c = 132$ marked the birth at the top of the flow system of a single vortex due to the combination of the predominant centrifugal forces and the Ekman layer at the top end-plate where the radii were the largest. The basic meridional flow was upward along the rotating wall and downward along the fixed one. The first observed vortex rotated inwards to the upper end-plate and formed with the basic flow a pair of

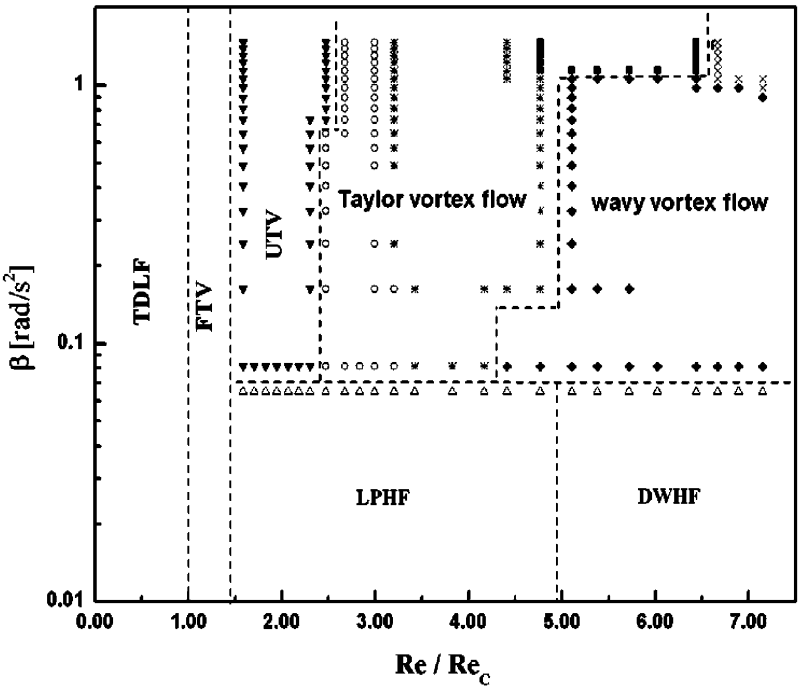

Fig. 2. Bifurcation diagram presenting flow state selection when the acceleration rate changes in the range of $\mathrm{Re}/\mathrm{Re}_c$ lower than 8.00. TDLF is the basic three-dimensional flow state, FTV is the state with the first observed vortices, and UTV is the flow state with upward traveling vortices.

counter-rotating vortices. When the inner conical cylinder rotational speed was increased slightly, counter-rotating vortex pairs appeared below the first observed vortex until they occupied almost three-quarters of the fluid column. This flow state is denoted by FTV in Fig. 2.

Depending on the acceleration rate β imposed, transition branching occurred when Re was increased. For values of $\beta > 0.06\,\mathrm{rad/s^2}$, the first observed vortices moved upward in a global motion (UTV state in Fig. 2) and filled the whole fluid column, leading to Taylor vortex flow modes when the Reynolds number was further increased, as discussed by Noui-Mehidi et al. (2002). For low acceleration rates of $\beta < 0.06\,\mathrm{rad/s^2}$, a helical flow propagated downward from the largest radius to the lowest one at a Reynolds number of $\mathrm{Re}/\mathrm{Re}_c = 1.47$.

3.2. Laminar helical flow

As stated in the previous section, the helical flow (denoted by LPHF) settled at $\mathrm{Re}/\mathrm{Re}_c = 1.47$ for very low accelerations of $\beta < 0.06\,\mathrm{rad/s^2}$. This flow structure is characterized by a pair of counter-rotating vortex tubes winding around the inner conical cylinder. To a stationary observer, the helical vortices, counter-rotating two by two, have a downward motion from the largest radius to the lowest one in the conical system.

Fig. 3 shows a front view and a laser section of the helical flow for $\mathrm{Re}/\mathrm{Re}_c = 1.52$. It can be seen from the laser section in Fig. 3(b) that the helical counter-rotating vortices have the same size within the gap. The front view in Fig. 3(a) shows that the helical vortices are inclined to the horizontal plane with a very small angle of 4°. The rotation of the helical structure around the inner conical cylinder acts like a coil to produce a 'barber-pole' effect on the vortices, with a constant velocity for a fixed Re. In the present flow system, the inner conical cylinder had a counterclockwise rotation, resulting in left-hand inclined helical vortices.

The signals collected for this flow state were periodic. The periodicity was the result of the downward axial drifting velocity of the helical vortices at the observation point, which is the measuring probe. At this flow state, due to the nature of the hydrodynamic structure observed, signals measured at all existing electrochemical probes showed similar

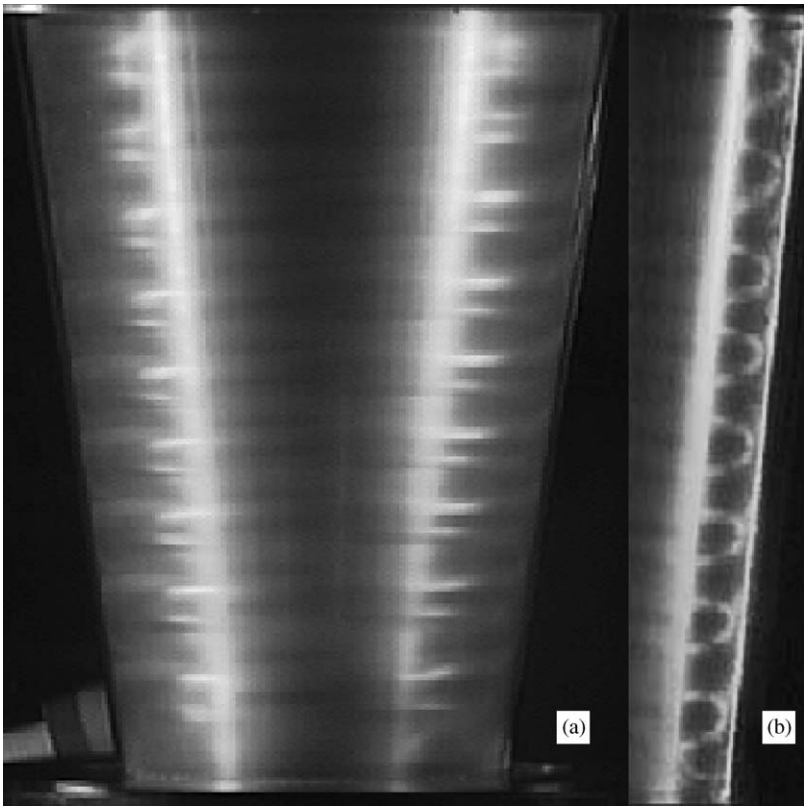

Fig. 3. Laminar periodic helical flow (LPHF): (a) front view, (b) Argon laser section view; $\mathrm{Re}/\mathrm{Re}_c = 1.52$.

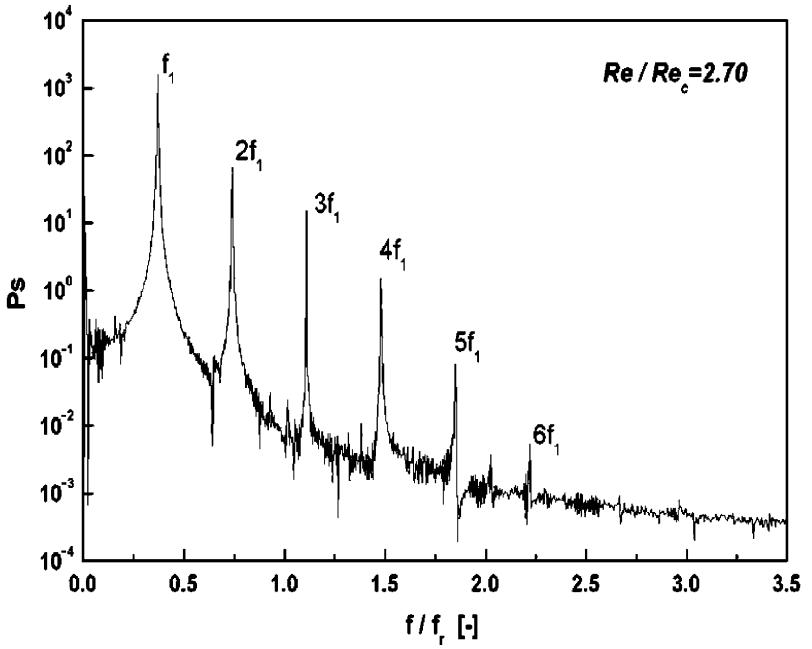

Fig. 4. Power spectrum in LPHF for $\mathrm{Re}/\mathrm{Re}_c = 2.70$.

time evolution and spectral properties. The results presented in the following correspond to measurements done at the probe located near the middle of the fluid column.

An adequate amplification raised the signal amplitude to a level that could be clearly visualized as a waveform on the digital recorder display. The power spectra obtained from the time series showed the single-periodic nature of the helical flow, as seen in Fig. 4 for $\mathrm{Re}/\mathrm{Re}_c = 2.70$. All power spectra collected revealed a sharp fundamental frequency f_1 peak with some harmonics. The fundamental frequency f_1 is related to the constant period of the measured signal due to the regular passage of the helical vortices by the measuring probe. When an outflow boundary passed near the measuring probe, the amplitude of the signal reached a maximum; then, when the following inflow boundary passed near the probe, the signal amplitude reached a minimum value.

When Re was increased further, the axial drifting velocity of the helical vortices became faster. The power spectra obtained at different Reynolds numbers for this flow regime showed that f_1 had a ratio of 0.36 to the inner conical cylinder rotation frequency, with an accuracy of 5%. This ratio was independent of the acceleration imposed on the inner cylinder rotation, as long as $\beta < 0.06\,\mathrm{rad/s^2}$. The effect of acceleration only seemed to be important at the onset of the helical flow.

3.3. Doubly periodic wavy helical flow

When Re was further increased, the axial velocity of the helical flow became faster. Visually, it was difficult to clearly discern the structure of the helical vortices. The signal analysis indicated a change in the helical flow at $\mathrm{Re}/\mathrm{Re}_c = 4.90$. The raw signals were still periodic, with a change in the waveform showing other small fluctuations due to the presence of azimuthal undulations superimposed to the helical motion. While direct visualization of these undulations was difficult, a video recorded with a digital camera and played in slow motion clearly showed the azimuthal waves, which translated the undulation of the counter-rotating helical vortices boundaries in the azimuthal direction with very small amplitudes, while moving downwards.

The power spectra collected contained the fundamental frequency $f_1$with its harmonics and a second fundamental frequency f_2 with several peaks resulting from combinations of f_1 and f_2, as can be seen in Fig. 5.

The presence of a second fundamental frequency f_2 is related to the azimuthal wavy motion superimposed to the helical downward flow. The appearance of the frequency f_2 at a value higher than the fundamental frequency f_1 (Fig. 5) is supported by the wavelet analysis of the collected time series in this flow state. The iso-correlation contour plots in

Fig. 6 show that there are two main structures: at time scales $a/\Delta t$ between 8.5 and 10.5, the regular high correlation form corresponds to the fundamental helical flow of f_1. While at time scales $a/\Delta t$ between 3.5 and 5.5 (i.e. higher frequencies) a second correlation waveform appears to be weak with regard to the previous one. The second correlation waveform corresponds to the azimuthal waves with f_2 attached to the helical flow.

Fig. 6 reveals also a competition between the azimuthal waves and the helical motion since the temporal evolution of the second correlation waveform, appearing at time scales $a/\Delta t$ between 3.5 and 5.5, is not steady. On the other hand, the presence of a multitude of frequency peaks resulting from combinations of f_1 and f_2 (Fig. 5) translated a constant offset of f_2-related peaks from the main fundamental frequency f_1. This property is due to the combination of the helical motion and the azimuthal undulations at the measuring fixed probe. In fact, the probe does not observe the azimuthal undulations at the same helical vortex but at a succession of helical vortices due to the downward axial drifting of the

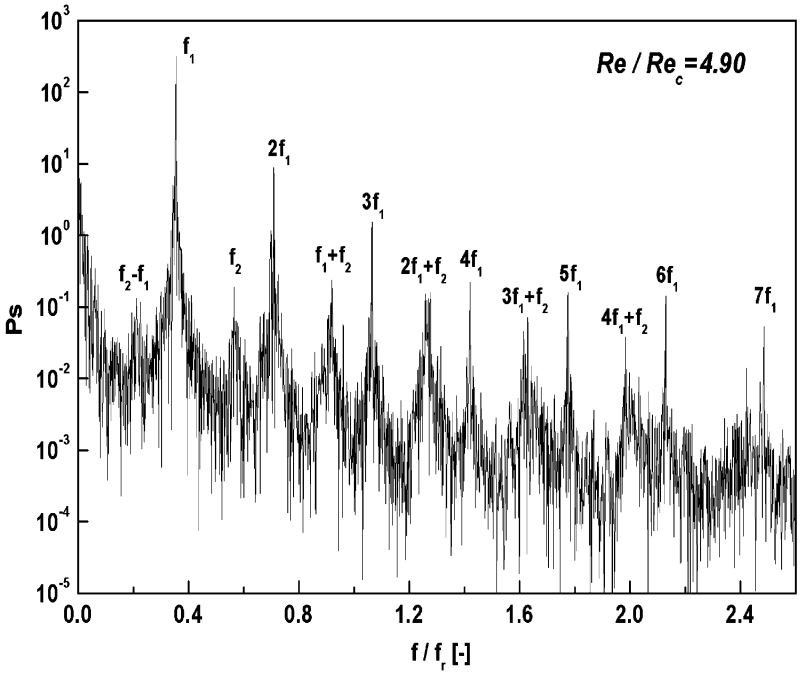

Fig. 5. Power spectrum in DWHF for $\mathrm{Re}/\mathrm{Re}_c = 4.90$.

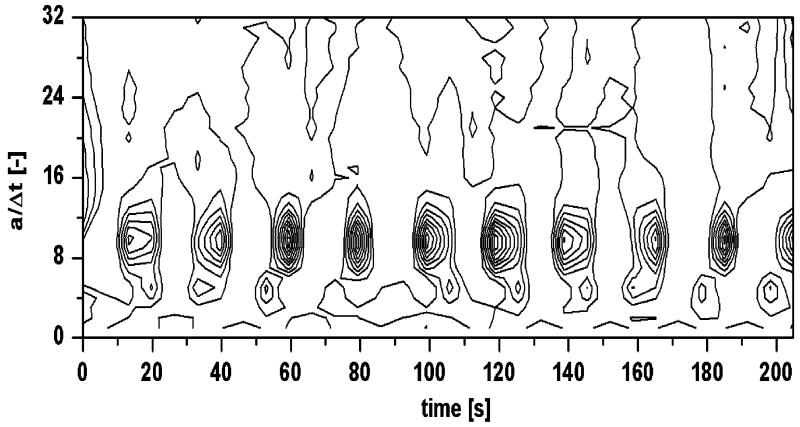

Fig. 6. Iso-correlation contour lines of the wavelet transform in DWHF for $\mathrm{Re}/\mathrm{Re}_c = 4.90$.

helical motion. Thus, the constant offset of the peaks related to f_2 from the corresponding f_1 peak is the result of the constant shift between portions of the azimuthal waves, each recorded at a helical vortex succeeding the previous one.

The frequency analysis showed that f_2 had a rational ratio to the helical flow f_1, as seen in the power spectrum of Fig. 5, where f_1 still has the same ratio of 0.36 to the inner conical cylinder frequency f_r. The flow state (denoted by DWHF) was then doubly periodic since the two fundamental frequencies f_1 and f_2 are independent.

Similar to the present flow regime, wavy-spiral regimes have been observed in the system of Taylor–Couette between circular cylinders. Chossat and Ioos (1994) found theoretically that this flow regime is the result of bifurcation solutions from spirals when both cylinders counter-rotate. The wavy-spiral flow regime between circular cylinders is quasiperiodic with two independent frequencies, the first linked to the basic spirals and the other one to the wavy motion. Andereck et al. (1986) observed this flow state experimentally for counter-rotating circular cylinders and called it wavy interpenetrating spirals. They also found that this flow state is not as well defined visually as the known wavy-vortex flow. However, the power spectra they obtained in this flow state did not point out any frequency linked to the wavy pattern.

3.4. Weakly turbulent helical flow

At a Reynolds number of $\mathrm{Re}/\mathrm{Re}_c = 14.70$, the frequency related to the azimuthal waves could not be seen any more in the power spectra. The azimuthal waves disappeared completely, due to the strong downward helical flow and to the additional presence of fluctuations of chaotic type. The power spectrum of Fig. 7 clearly illustrates this fact and shows that this flow state corresponds to a weakly turbulent helical flow (WTHF). The power spectrum contains a lot of noise and the helical flow fundamental frequency f_1 is still preponderant in the spectrum, with only two remaining harmonics. The fundamental frequency f_1 has the same ratio of 0.36 to the inner conical cylinder rotation frequency in the range of $\mathrm{Re}/\mathrm{Re}_c$ between 14.70 and 37.50. When Re was increased, the fluctuations became stronger. Power spectra collected for $\mathrm{Re}/\mathrm{Re}_c > 37.50$ showed that the ratio of f_1 to the rotational frequency was not constant any more, and increased as $\mathrm{Re}/\mathrm{Re}_c$ increased. This property is supported by the power spectra shown in Fig. 8 and the frequency evolution with $\mathrm{Re}/\mathrm{Re}_c$ shown in Fig. 9. It can be seen from Fig. 9 that the continuous increases of the ratio f_1/f_r became very sharp for $\mathrm{Re}/\mathrm{Re}_c$ between 49.70 and 66.50.

The increase of the frequency ratio f_1/f_r is due to the high competition between the basic helical motion and the presence of flow fluctuations, which become stronger as the rotational speed of the inner conical cylinder increases. The

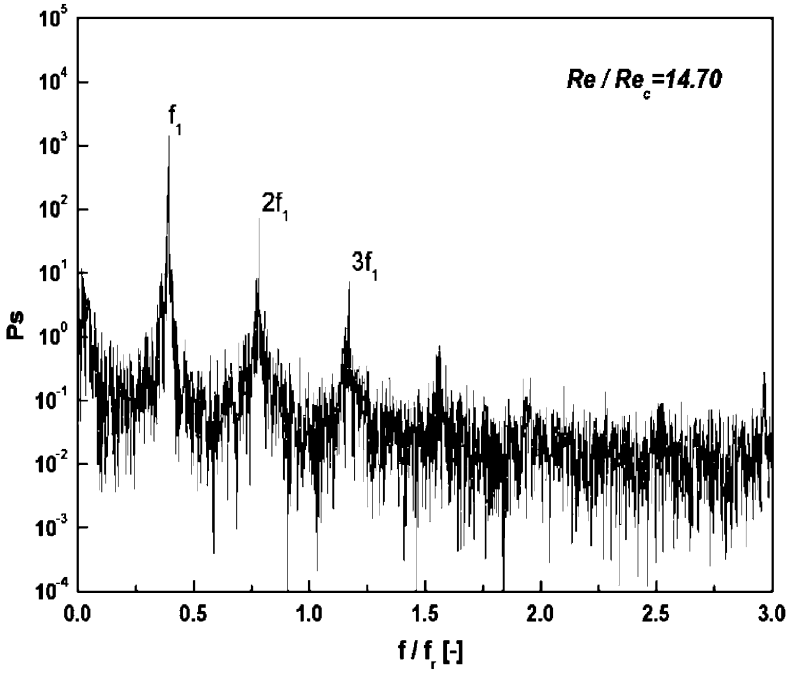

Fig. 7. Power spectrum in WTHF for $\mathrm{Re}/\mathrm{Re}_c = 14.70$.

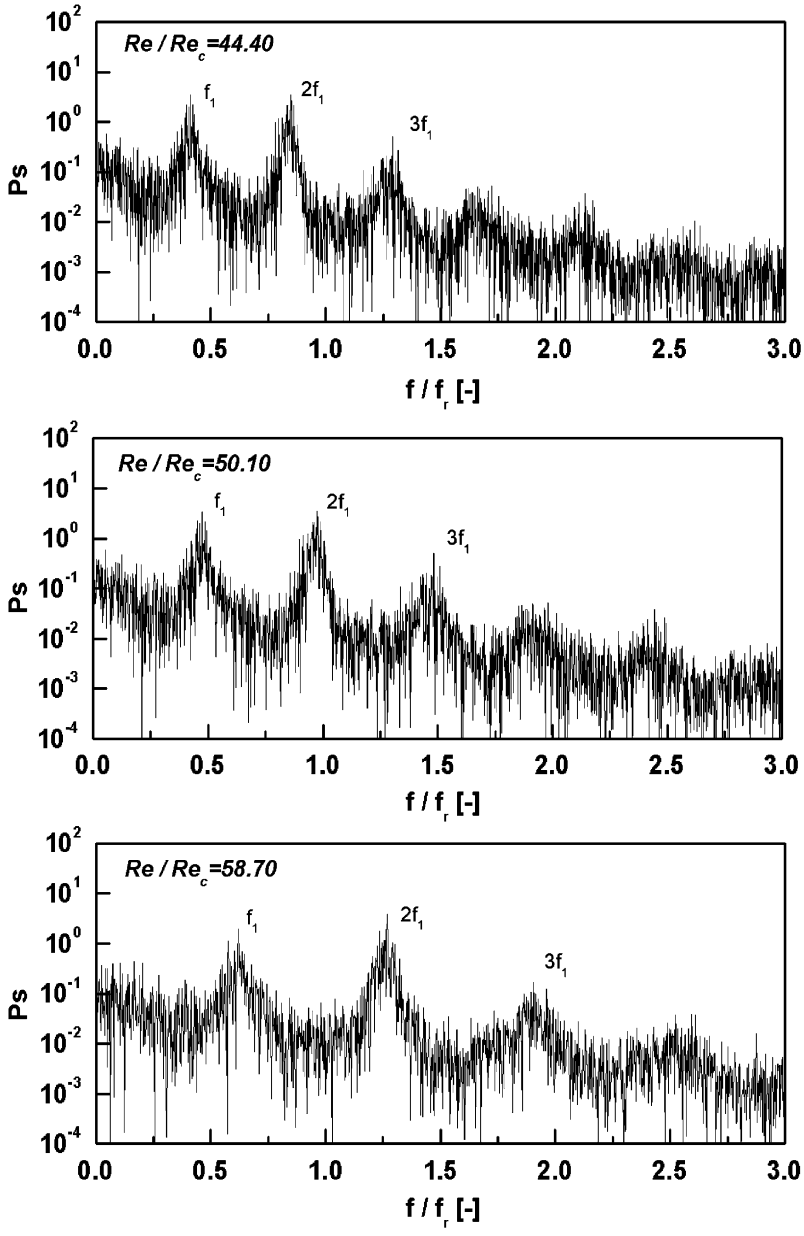

Fig. 8. Power spectra change in WTHF as $\mathrm{Re}/\mathrm{Re}_c$ increased.

strong flow fluctuations favor the transfer of energy to small scales, which increase the spatial freedom of the flow system and thus enhance the transportation energy of the helical wave.

3.5. Fully turbulent helical flow

The value of $\mathrm{Re}/\mathrm{Re}_c = 66.50$ marked the settling of a fully turbulent flow regime (abbreviated as FTHF). Visually the flow seemed to be completely chaotic, with a very fast downward motion in which the boundaries of the helical vortices could not be observed. Signal analysis revealed the existence of the fundamental helical train with a high-frequency ratio f_1/f_r. Power spectra collected in the range $\mathrm{Re}/\mathrm{Re}_c$ between 66.50 and 118.30 have shown that the ratio f_1/f_r reached another fixed value of 0.81, as supported by Fig. 9. An example of the turbulent

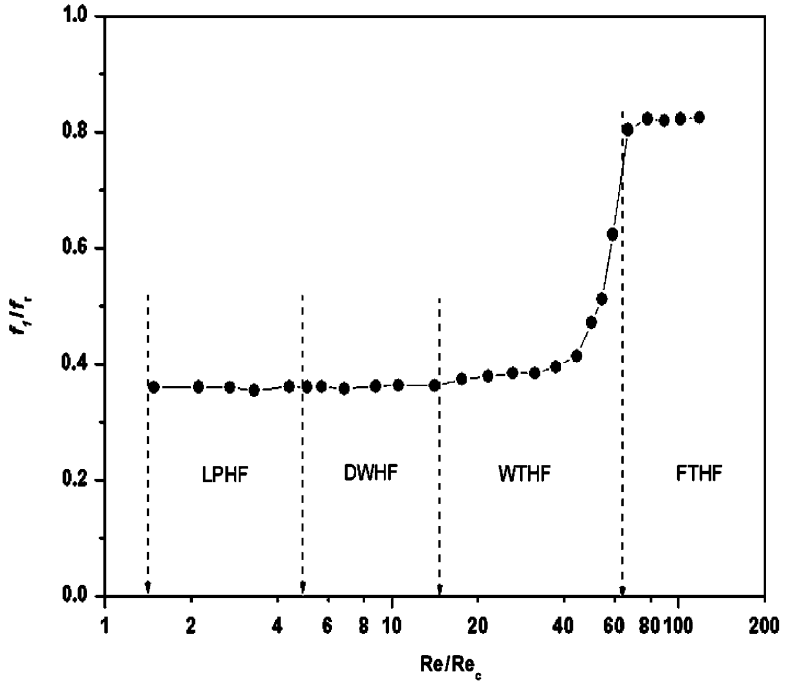

Fig. 9. Evolution of the helical flow fundamental frequency f_1 as the Reynolds number increases.

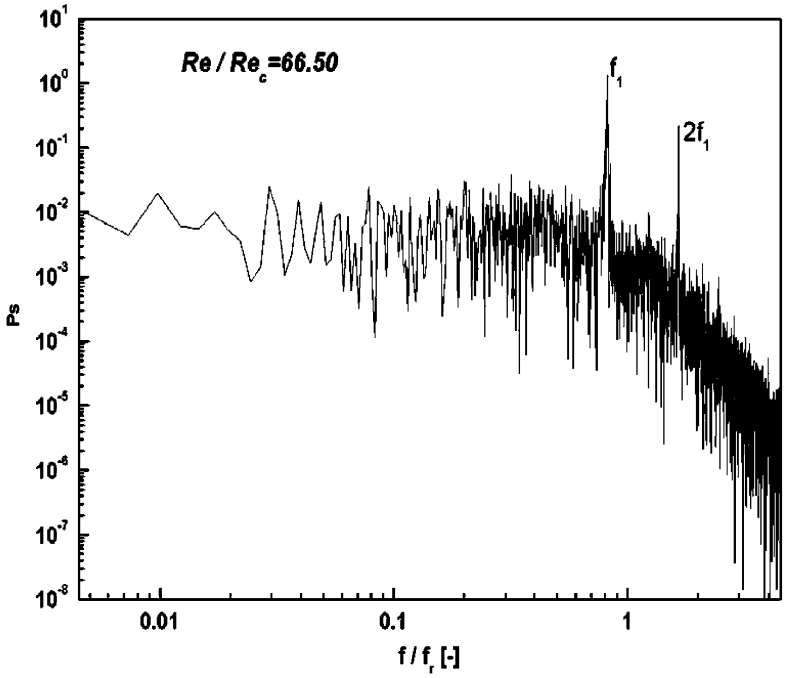

Fig. 10. Power spectrum in FTHF for $\mathrm{Re}/\mathrm{Re}_c = 66.50$.

power spectra is shown in Fig. 10. A logarithmic representation pointed out a very sharp frequency f_1 with only one harmonic.

The contour plots of the wavelet transform iso-correlations shown in Fig. 11 indicate that the helical structure is not temporally steady as previously seen in Fig. 6. Although high correlation forms are still observed at time scale $a/\Delta t$

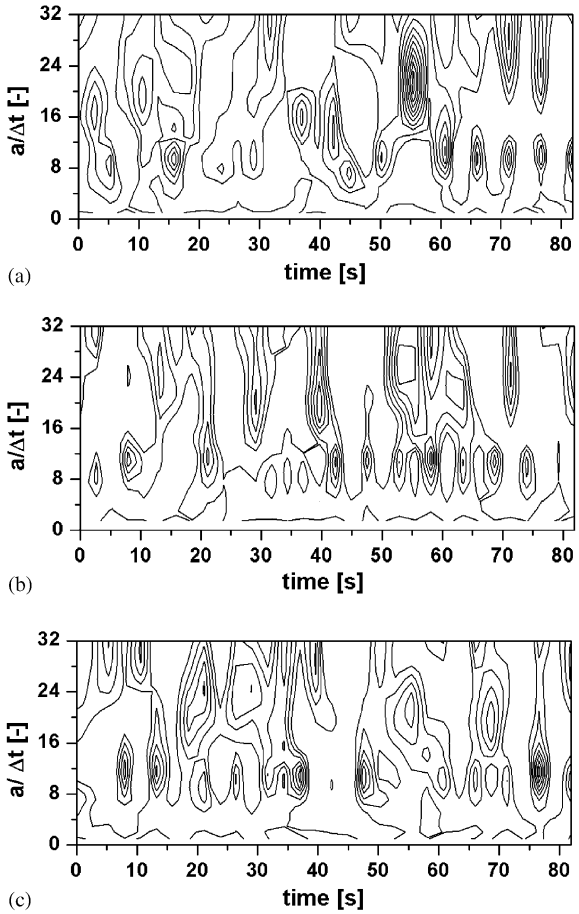

Fig. 11. Iso-correlation contour lines of the wavelet transform in FTHF for: (a) $\mathrm{Re}/\mathrm{Re}_c = 66.50$, (b) $\mathrm{Re}/\mathrm{Re}_c = 88.70$, (c) $\mathrm{Re}/\mathrm{Re}_c = 118.50$.

between 8.5 and 12.5, the forms are irregular in time, revealing the existence of a strong competition between the basic helical flow and the chaotic fluctuations introducing other high correlation values.

4. Phase space analysis

The phase space study in bifurcation problems gives important information on the type of bifurcation that occurs in a dynamical system when one or more dominant parameters are changed. The phase portraits constructed from the normalized fluctuating component of the recorded signals permitted the identification of the type of bifurcation leading to the succession of the different observed flow regimes.

In the LPHF regime, the attractor construction showed a pure limit cycle presented in Fig. 12(a), which suggests that the helical flow transition occurred with a Hopf bifurcation type from the first observed vortices flow regime. A second Hopf bifurcation occurred in the transition to the DWHF flow state. The attractor constructed from the time series shown in Fig. 12(c) and the Poincaré section of Fig. 12(d) suggest that the orbit lies on the surface of a torus where the dominating frequency is f_1 and the second frequency is f_2. This transition is similar to the one observed in the Taylor–Couette system in the transition of singly periodic wavy-vortex flow to doubly periodic wavy-vortex flow, which results from a Hopf bifurcation (Ohmura et al., 1995). The phase space analysis of the WTHF regime shows that the torus does not exist anymore. Since the flow is dominated by the helical basic flow, the noise induced by the chaotic fluctuations results in a noisy cycle, which is still evident. In the perturbed cycle, the orbits are continuously deviating

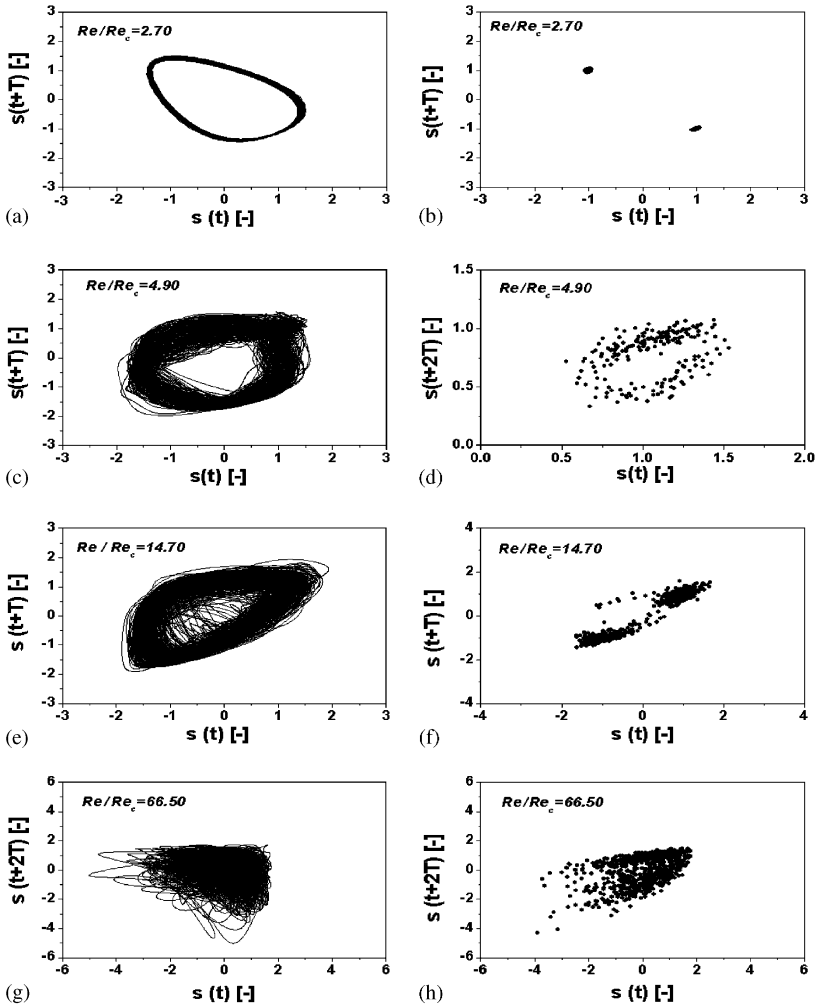

Fig. 12. Phase space portraits (left) and Poincaré sections (right) and delay times T in: (a) and (b) LPHF, $T = 2.30$; (c) and (d) DWHF, $T = 1.80$; (e) and (f) WTHF, $T = 1.34$; (g) and (h) FTHF, $T = 1.28$. The Poincaré planes are: (b) $s(t + 2T) = 0$, (d) $s(t) = 0$, (f) $s(t + 2T) = 0$ and (h) $s(t + T) = 0$.

from the fundamental limit cycle corresponding to the basic helical flow, as seen in the phase portrait of Fig. 12(e) and the Poincaré section of Fig. 12(f). The transition to the WTHF regime in the present study seems to be characteristic of the conical flow system. While in the Taylor–Couette flow system the torus motion breaks up in the process to the generation of chaotic turbulence, in the present system the torus motion breaks up to a kind of irregular limit cycle. An increase of Reynolds number generates more chaotic fluctuations, leading to a fully turbulent flow (FTHF) characterized by a strange attractor, as shown in Fig. 12(g) and the Poincaré section in Fig. 12(h).

5. Conclusions

The transition of laminar helical flow to turbulent helical flow in a system formed by two coaxial conical cylinders was investigated experimentally. Signal analysis performed on time series recorded from fluctuations of the wall gradient velocity revealed a transition scenario specific to the present flow system. When the Reynolds number was increased, the singly periodic helical flow was replaced by a doubly periodic wavy helical flow, with two independent

fundamental frequencies revealing the existence of a torus in the phase space. For higher Reynolds numbers, the wavy flow disappeared due to the settling of fluctuations of chaotic type, and the flow degenerated to a fully turbulent motion. The ratio of fundamental frequency to rotational frequency increased sharply before turbulent flow occurred. The wavelet transform showed that the helical flow, still existing in the turbulent regime, was affected by fluctuations of high order of magnitude. The present study and previous studies have shown that the flow between conical cylinders revealed diversified routes towards chaos with characteristic properties that need further investigation both experimentally and theoretically.

References

Andereck, C.D., Liu, S.S., Swinney, H.L., 1986. Flow regimes in a circular Couette system with independently rotating cylinders. Journal of Fluid Mechanics 164, 155–183.

Antonijoan, J., Marques, F., Sanchez, J., 1998. Nonlinear spirals in the Taylor–Couette problem. Physics of Fluids 10, 829–838.

Chossat, P., Ioos, G., 1994. The Couette–Taylor Problem. Springer, New York.

Cognet, G., 1971. Utilisation de la polarographie pour l'étude de l'écoulement de Couette. Journal de Mécanique 10, 65–90.

Fraser, A.M., Swinney, H.L., 1986. Independent coordinates for strange attractors from mutual information. Physical Review A 33, 1134–1140.

Hoffmann, N.P., Busse, F.H., 1999. Instabilities of shear flows between two coaxial differentially rotating cones. Physics of Fluids 11, 1676–1678.

Hoffmann, C., Lücke, M., 2000. Spiral vortices and Taylor vortices in the annulus between counter-rotating cylinders. In: Egbers, C., Pfister, G. (Eds.), Physics of Rotating Fluids. Springer, Berlin, pp. 55–66.

Meseguer, A., Marquès, F., 2000. On the competition between centrifugal and shear instability in spiral Couette flow. Journal of Fluid Mechanics 402, 33–56.

Noui-Mehidi, M.N., Wimmer, M., 1999. Free surface effects on the flow between conical cylinders. Acta Mechanica 135, 13–25.

Noui-Mehidi, M.N., Ohmura, N., Kataoka, K., 2001. An experimental investigation of flow mode selection in a conical Taylor Couette system. International Journal of Fluid Dynamics 5, 1–16.

Noui-Mehidi, M.N., Ohmura, N., Kataoka, K., 2002. Mechanism of mode selection for Taylor vortex flow between coaxial conical rotating cylinders. Journal of Fluids and Structures 16, 247–262.

Ohmura, N., Kataoka, K., Mizumoto, T., Nakata, M., Matsumoto, K., 1995. Effect of vortex cell structure on bifurcation properties in a Taylor vortex flow system. Journal of Chemical Engineering of Japan 28, 758–764.

Park, S.H., Kang, Y., Cho, Y.J., Fan, L.T., Kim, S.D., 2001. Characterization of pressure signals in a bubble column by wavelet transform. Journal of Chemical Engineering of Japan 34, 158–165.

Wimmer, M., 1995. An experimental investigation of Taylor vortex flow between conical cylinders. Journal of Fluid Mechanics 292, 205–227.

Wimmer, M., 2000. Taylor vortices at different geometries. In: Egbers, C., Pfister, G. (Eds.), Physics of Rotating Fluids. Springer, Berlin, pp. 195–212.

Zheng, J., Kishimoto, S., Ochi, T., Yoshimura, T., Ohmura, N., Kataoka, K., 2001. Flow mechanism of a submerged jet impinging on a free interface. Journal of Chemical Engineering of Japan 34, 912–918.